THE ASTROPHYSICAL JOURNAL, 545:827–841, 2000 December 20

THE SUPERGIANT SHELL LMC 2. II. PHYSICAL PROPERTIES OF THE 10^6 K GAS

S. D. POINTS AND Y.-H. CHU
Astronomy Department, University of Illinois, 1002 W. Green Street, Urbana, IL 61801
S. L. SNOWDEN[1]
NASA Goddard Space Flight Center, Laboratory for High Energy Astrophysics, Code 662, Greenbelt, MD 20771
AND
L. STAVELEY-SMITH
Australia Telescope National Facility, CSIRO, P.O. Box 76, Epping, NSW 2121, Australia
Received 2000 June 21; accepted 2000 August 18

ABSTRACT

LMC 2 has the highest X-ray surface brightness of all known supergiant shells in the Large Magellanic Cloud (LMC). The X-ray emission peaks within the ionized filaments that define the shell boundary but also extends beyond the southern border of LMC 2 as an X-ray bright spur. *ROSAT* HRI images reveal the X-ray emission from LMC 2 and the spur to be truly diffuse, indicating a hot plasma origin. We have obtained *ROSAT* PSPC and *ASCA* SIS spectra to study the physical conditions of the hot ($\geq 10^6$ K) gas interior to LMC 2 and the spur. Raymond-Smith thermal plasma model fits to the X-ray spectra, constrained by H I 21 cm emission line measurements of the column density, show the plasma temperature of the hot gas interior of LMC 2 to be $kT \sim 0.1$–0.7 keV and of the spur to be $kT \sim 0.1$–0.5 keV. We have compared the physical conditions of the hot gas interior to LMC 2 with those of other supergiant shells, superbubbles, and supernova remnants (SNRs) in the LMC. We find that our derived electron density for the hot gas inside LMC 2 is higher than the value determined for the supergiant shell LMC 4, comparable to the value determined for the superbubble N11, and lower than the values determined for the superbubble N44 and a number of SNRs.

Subject headings: ISM: bubbles — ISM: individual (LMC 2) — X-rays: ISM

1. INTRODUCTION

Supergiant shells with sizes approaching 1000 pc form the largest structures seen in the interstellar medium (ISM). Such shells have been detected in the H I 21 cm and Hα lines in our Galaxy, Local Group galaxies, and more distant galaxies (Tenorio-Tagle & Bodenheimer 1988). These supergiant shells contain 10^{51}–10^{54} ergs of kinetic energy, which is most likely contributed by multiple supernovae and energetic stellar winds over several dozen Myr. The size of a supergiant shell often exceeds the scale height of the gaseous disk of its host galaxy, thus forming a "chimney" through which energy and mass flow into the galaxy's halo. Therefore, supergiant shells play important roles in the global evolution of the ISM in a galaxy.

It is difficult to study supergiant shells in detail. Their distances, and thus their sizes and energies, remain uncertain in our Galaxy; furthermore, interstellar obscuration often prevents observations at optical, UV, and X-ray wavelengths. For distant galaxies, angular resolution becomes a severe limiting factor. The Large Magellanic Cloud (LMC) offers a happy compromise, as it is close (50 kpc; Feast 1999) and has little obscuration ($A_V < 0.3$ mag; Bessell 1991).

Nine supergiant shells with sizes ranging from 600 to 1400 pc have been reported in the LMC, LMC 1–9 (Goudis & Meaburn 1978; Meaburn 1980). Only two of these shells have been studied in detail, LMC 2 and LMC 4, because LMC 2 is the most spectacular and LMC 4 is the largest. Both supergiant shells are filled with hot plasma: diffuse X-ray emission has been detected in LMC 2 by Wang & Helfand (1991) using *Einstein* Imaging Proportional Counter (IPC) data and in LMC 4 by Bomans, Dennerl, & Kürster (1994) with a 46 ks *ROSAT* Position Sensitive Proportional Counter (PSPC) observation. LMC 2 is substantially brighter in X-rays than LMC 4 and all other supergiant shells in the LMC.

The physical and kinematic structure of LMC 2 has been reported by Points et al. (1999, hereafter Paper I). It is found that two different mechanisms are responsible for generating the X-ray–emitting plasma: (1) local heating by supernova remnants (SNRs), e.g., the emission region enclosed by the northeast rim; and (2) outflows from active star formation regions, e.g., the bright X-ray arc extending from N158 (notation from Henize 1956) to N159 (or SNR 0540−693 to LMC X-1; see Fig. 1*b*). The south end of LMC 2 is confusing. Diffuse X-ray emission, while peaking within the shell, extends beyond the southern border of LMC 2. It has been speculated that this X-ray spur represents a blowout of LMC 2, but no optical or radio supporting evidence has been found.

LMC 2 clearly demonstrates the existence of hot gas interior to a supergiant shell and illustrates different mechanisms of generating the hot gas. Spatially resolved spectral analysis of the X-ray emission within LMC 2 and neighboring regions is the most effective way to determine the physical conditions of the hot plasma and establish its role in the multiphase interstellar medium.

The X-ray emission from the interior of LMC 2 has not been studied since its initial detection with the *Einstein* IPC. Those IPC data were not used to make a detailed spectral analysis, however, because they had low spectral resolution and were contaminated by hard X-rays scattered from LMC X-1 to large off-axis angles (Wang & Helfand 1991). To study the distribution of X-ray emission toward LMC 2, we have obtained *ROSAT* PSPC and High Resolution

[1] Universities Space Research Association.

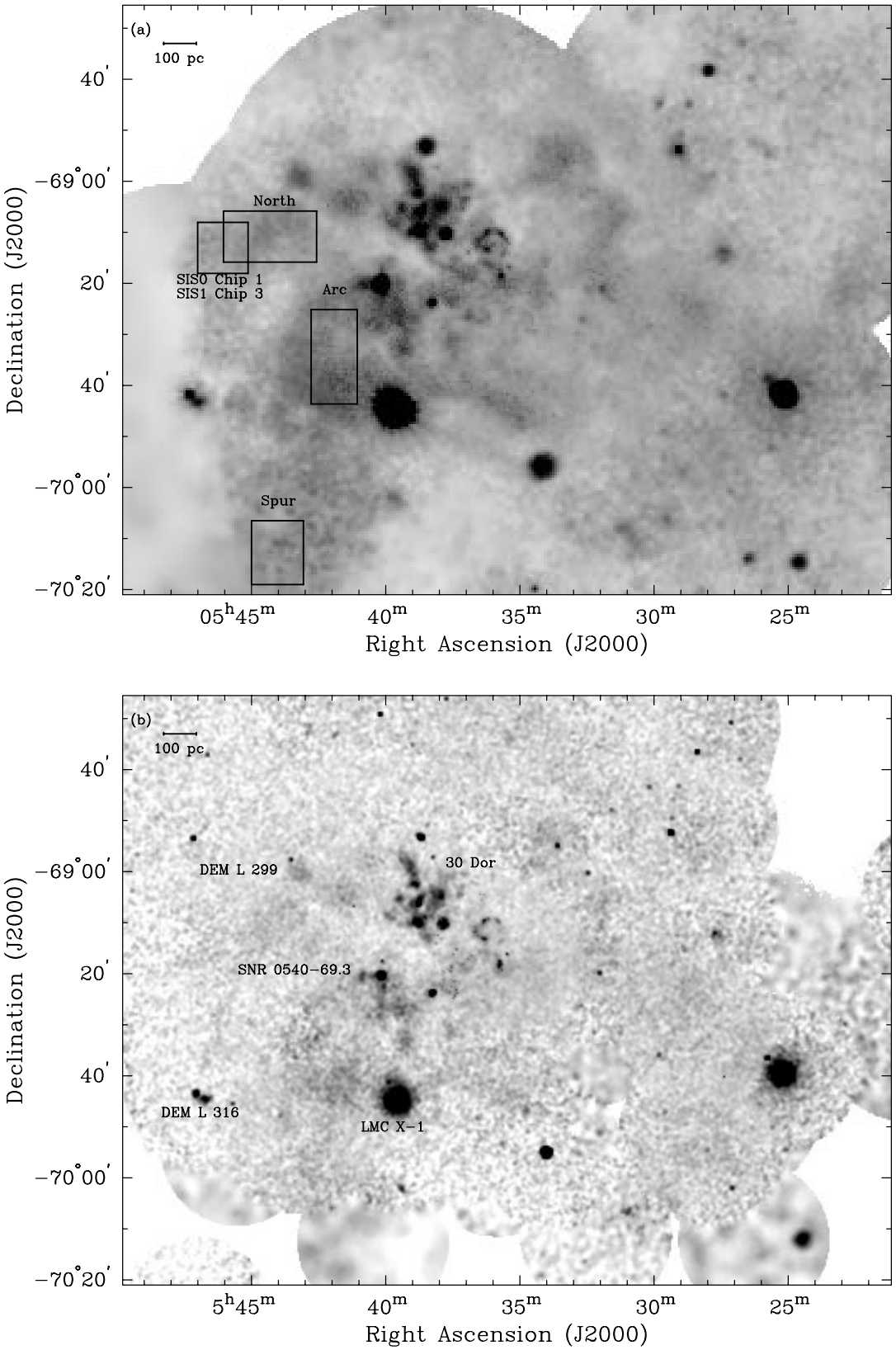

FIG. 1.—(*a*) *ROSAT* PSPC mosaic of the LMC 2 region in the R4–R7 bandpass with the areas from which spectra were extracted labeled. (*b*) *ROSAT* HRI mosaic of the LMC 2 region with X-ray sources mentioned in the text labeled.

Imager (HRI) observations of LMC 2. Furthermore, to determine the physical conditions of the X-ray–emitting plasma interior to LMC 2, we have also obtained *ASCA* Solid-State Imaging Spectrograph (SIS) observations.

This paper is organized as follows. Section 2 describes the observations used in this study and their reduction. The distribution of the hot ($\geq 10^6$ K) plasma and its relationship to the warm ($\sim 10^4$ K) and cold ($\sim 10^2$ K) interstellar component of LMC 2 are discussed in § 3. In § 4 we describe the physical condition of the hot gas. In § 5 we compare the physical properties of LMC 2 with other objects that exhibit diffuse X-ray emission. We summarize our results in § 6.

2. OBSERVATIONS AND DATA REDUCTION

The X-ray data reported in this paper were obtained using the *ROSAT* PSPC and HRI and the *ASCA* SIS.

2.1. *X-Ray Images*

The X-ray images of LMC 2 were obtained with the *ROSAT* X-ray telescope, using both the PSPC and the HRI. As discussed in Paper I, we have mosaicked a large number of independent PSPC and HRI observations to provide extensive angular coverage and considerably deeper exposure than provided by the *ROSAT* All-Sky Survey (RASS). The data were retrieved through the *ROSAT* public archive at the High Energy Astrophysics Science Archive Research Center (HEASARC) at the Goddard Space Flight Center. The region surrounding LMC 2 has been extensively covered by PSPC observations of the many sources in the vicinity (e.g., SNRs and X-ray binaries) and by the HRI survey program of Chu & Snowden (1996), which was designed to cover the 30 Doradus and bar regions of the LMC with deep and uniform coverage. Tables A1 and A2 list the observation sequences that were used for the mosaics of the PSPC and HRI, respectively (see the Appendix). These tables include the number of data sets for each sequence (individual observations were occasionally processed in sections), pointing direction, exposure time, and target name. The data reduction was accomplished using the Extended Source Analysis Software (ESAS) package (Snowden & Kuntz 1998; Kuntz & Snowden 1998), which is also available through the HEASARC. The final PSPC and HRI mosaics are cast in the same projection with the field center at $(\alpha, \delta)_{2000} = (5^h42^m, -69°30')$ and pixel size of 30″ and 20″, respectively. The projection is the zenith equal-area azimuthal (ZEA; Greisen & Calabretta 1995), which is similar over this solid angle to the more common tangential projection.

2.1.1. *PSPC Mosaic*

Reduction of the PSPC data followed the procedures outlined by Snowden et al. (1994) and demonstrated by Snowden & Petre (1994) and in fact included a reprocessing of data in the latter paper. Individual observations were screened for anomalous background conditions, had their residual non–cosmic background components modeled and subtracted, and had their vignetted and deadtime-corrected exposures calculated. Only after all of the individual observations were reduced in six statistically independent energy bands (see Table 1) were they cast into the mosaics. Because the analysis software cannot correct for zero-level offsets (a constant component of the long-term enhancement non–cosmic background; see Snowden et al. 1994), the mosaicking process must correct for the relative offsets between overlapping fields. A single-value deconvolution algorithm was applied to a system of equations comprising all overlaps between separate observations to determine a best fit for all offsets simultaneously. A final constraint was added so that the sum of the offsets was equal to zero. Individual observations were then adjusted by multiplying the fitted offset by the exposure map to produce an offset count image, which was then subtracted from the count image. This procedure was run separately on each energy band. Table 2 lists some values of interest for the reduction. The true source counts can be seen to completely dominate the non–cosmic background, and the average exposures are larger by more than an order of magnitude than that of the RASS coverage. Although these source counts include emission from 30 Doradus, LMC X-1, and various SNRs, LMC 2 is well above non–cosmic background. The total coverage of the field is ~ 18.2 deg^2. We have extracted a ~ 4.5 deg^2 subimage of the LMC 2 region from the larger mosaic and present it in Figure 1*a*.

TABLE 1

BROAD ENERGY BAND DEFINITIONS

Band Name	PI Channels	Energy[a] (keV)
R1	8–19	0.11–0.284
R2	20–41	0.14–0.284
R4	52–69	0.44–1.01
R5	70–90	0.56–1.21
R6	91–131	0.73–1.56
R7	132–201	1.05–2.04

[a] 10% of peak response.

2.1.2. *HRI Mosaic*

The reduction of HRI data is simplified from that of PSPC data. There is only the total energy band, and only the particle background is modeled and removed. The particle background of the HRI completely dominates an HRI observation with an average count rate $\sim$5–10 times greater than the cosmic background. It must be removed as the distribution of the particle background is flat across the field while cosmic counts are vignetted. Unfortunately, the particle background is also only calibrated to $\sim 10\%$ or so, but this is sufficient for the purposes of this paper. The contributions from other non–cosmic background components are ignored as they are "in the noise." Because these components are for the most part distributed as a vignetted flat field, they contribute a zero-level offset that is

TABLE 2

RELEVANT PARAMETERS OF THE X-RAY MOSAICS

Band	Average Exposure (ks)	Total Counts Observed	Total Counts Background	Average Intensity[a]
R4	25.12	289179	46063	255
R5	25.15	442372	19820	389
R6	24.65	655163	12646	410
R7	21.94	419176	13250	179
HRI.....	26.13	3149624	2346460	1032

[a] Units of 10^{-6} counts s^{-1} arcmin^{-2}.

corrected in the mosaicking, which is done in the same manner as for the PSPC. The total coverage of the field is ~ 8.1 deg^2. In Figure 1*b* we present a subimage from this mosaic that has the same field of view as Figure 1*a*.

2.2. *X-Ray Spectra*

The X-ray spectra in this paper were obtained with the *ROSAT* PSPC and the *ASCA* SIS. Here we discuss the reduction of the X-ray spectral data. We discuss their analysis in § 4.

2.2.1. *ROSAT PSPC Spectra*

We extract X-ray spectra of LMC 2 from a *ROSAT* PSPC observation of the SNR DEM L 316 (*ROSAT* Sequence RP500259N00). The PSPC is sensitive in the energy range of 0.1–2.4 keV and has an energy resolution of $\approx 43\%$ at 1 keV. This observation has been discussed in some detail in Williams et al. (1997). Therefore, we only present a brief summary here. The observation was made within the time interval from 1993 January 10 to 1993 February 10. For this observation, the SNR DEM L 316 ($\alpha_{2000} = 5^h47^m9^s.5$, $\delta_{2000} = -69°42'14''$) was centered in the PSPC. The total exposure time for the observation was 4.0 ks.

We processed these data using Xselect and FTOOLS,[2] which are available through the HEASARC. The data were spatially binned to produce $7''.5 \times 7''.5$ pixels. Using the binned PSPC image, we defined three regions of interest: a bright region in the northern part of LMC 2 (PSPC-North), a bright X-ray arc in the west (PSPC-Arc), and a region in the X-ray spur to the south of LMC 2 (PSPC-Spur). These regions are shown in Figure 1*a*. Because LMC 2 is an extended source and all the regions are located outside the central PSPC "ring" (radius 20′), we selected background regions of the same size and off-axis angle to correct for the charged particle background. During the reduction process, we also performed vignetting corrections. We present the regions' coordinates, angular sizes, net counts, and effective exposure times in Table 3.

2.2.2. *ASCA SIS Spectra*

Our *ASCA* observation is of a bright X-ray region in the northern section of LMC 2 (see Fig. 1*a*). This observation was performed on 1995 August 25–26 (*ASCA* Sequence 53039000).

The *ASCA* satellite consists of two instruments that observe simultaneously: a pair of SISs and a pair of Gas Imaging Spectrographs (GISs). The SIS has an energy coverage approximately in the 0.5–8 keV range and the GIS in the 0.8–10 keV range (Tanaka, Inoue, & Holt 1994). In this paper we have only used the SIS data because of the low sensitivity of the GIS for energies below ≈ 1.0 keV, where diffuse thermal plasma emission is brightest. The SIS detectors have good spectral resolution [$\delta E/E \sim 0.02(5.9\ \mathrm{keV}/E)^{0.5}$]. The angular resolution of the SIS data is poor compared to the *ROSAT* PSPC, with a narrow core of $\approx 1'$ diameter and a half-power radius of 3′. Both of the SIS detectors (SIS 0 and SIS 1) are composed of four separate CCDs. Not all of the CCDs can be on for a given observation as the presence of "hot" and "flickering" pixels can fill the telemetry with false signals.

Because of telemetry limitations, our observations were performed in the 2 CCD mode, with part of the bright northern region of LMC 2 in the SIS 0 (chips 0 and 1) and SIS 1 (chips 0 and 3). We have extracted spectra from SIS 0 chip 1 and SIS 1 chip 3 because they image the same area on the sky and lie in a region of bright emission. We reduced and processed the data with ASCASCREEN and FTOOLS. Because LMC 2 is more extended than the SIS field of view, no region from any of our *ASCA* observations was suitable to perform a background subtraction. Therefore, we used the *ASCA* Deep Field pointings, screened in a manner identical to the LMC 2 data, to obtain regions for background subtraction. In Table 3 we also present relevant information on the two *ASCA* SIS chips that were used in this paper. We have also extracted spectra in the regions covered by SIS 0 chip 0 and SIS 1 chip 0; however, these data were not analyzed because the count rates were low and these spectra cannot be fitted by models with reasonable certainty.

3. SPATIAL DISTRIBUTION OF THE ISM TOWARD LMC 2

LMC 2 consists of interstellar gas in several phases. As reported in Paper I, we have obtained (1) *ROSAT* PSPC and HRI mosaics to investigate the spatial distribution of the hot ionized gas interior to LMC 2, (2) CCD images of LMC 2 in optical emission lines to examine the shell of warm ionized gas, and (3) 21 cm H I data to study the structure of the cold, neutral gas. Below we describe the distribution of the X-ray–emitting plasma and its relation to the other gaseous components.

3.1. *Morphology of the Hot Ionized Medium of LMC 2*

The existence of hot ($\geq 10^6$ K) gas interior to LMC 2 was first detected using the *Einstein* IPC (Wang & Helfand 1991). As seen in our *ROSAT* PSPC and HRI mosaics (Figs. 1*a* and 1*b*, respectively), LMC 2 lies toward the brightest and most complex region of diffuse X-ray emission in the LMC. This region includes 30 Doradus, LMC 2, the supergiant shell LMC 3, and a bright X-ray spur to the

[2] These data were also reduced using the IRAF/PROS packages. No apparent differences exist between the resulting spectra.

TABLE 3

PARAMETERS OF THE EXTRACTION REGIONS

Region Name	R.A. (J2000)	Decl. (J2000)	Size (square arcmin)	Off-Axis Angle (arcmin)	Net Counts	Average Exposure (ks)
PSPC-North.....	5 44 19	−69 10 51	185	34.7	717	2.7
PSPC-Arc.....	5 41 55	−69 34 23	166.5	27.8	1255	2.7
PSPC-Spur	5 44 02	−70 12 46	123	34.2	512	2.8
SIS 0 chip 1	5 46 04	−69 13 03	108	8.4	3737	30.7
SIS 1 chip 3	5 46 04	−69 13 03	104	8.1	3382	30.7

NOTE.—Units of right ascension are hours, minutes, and seconds, and units of declination are degrees, arcminutes, and arcseconds.

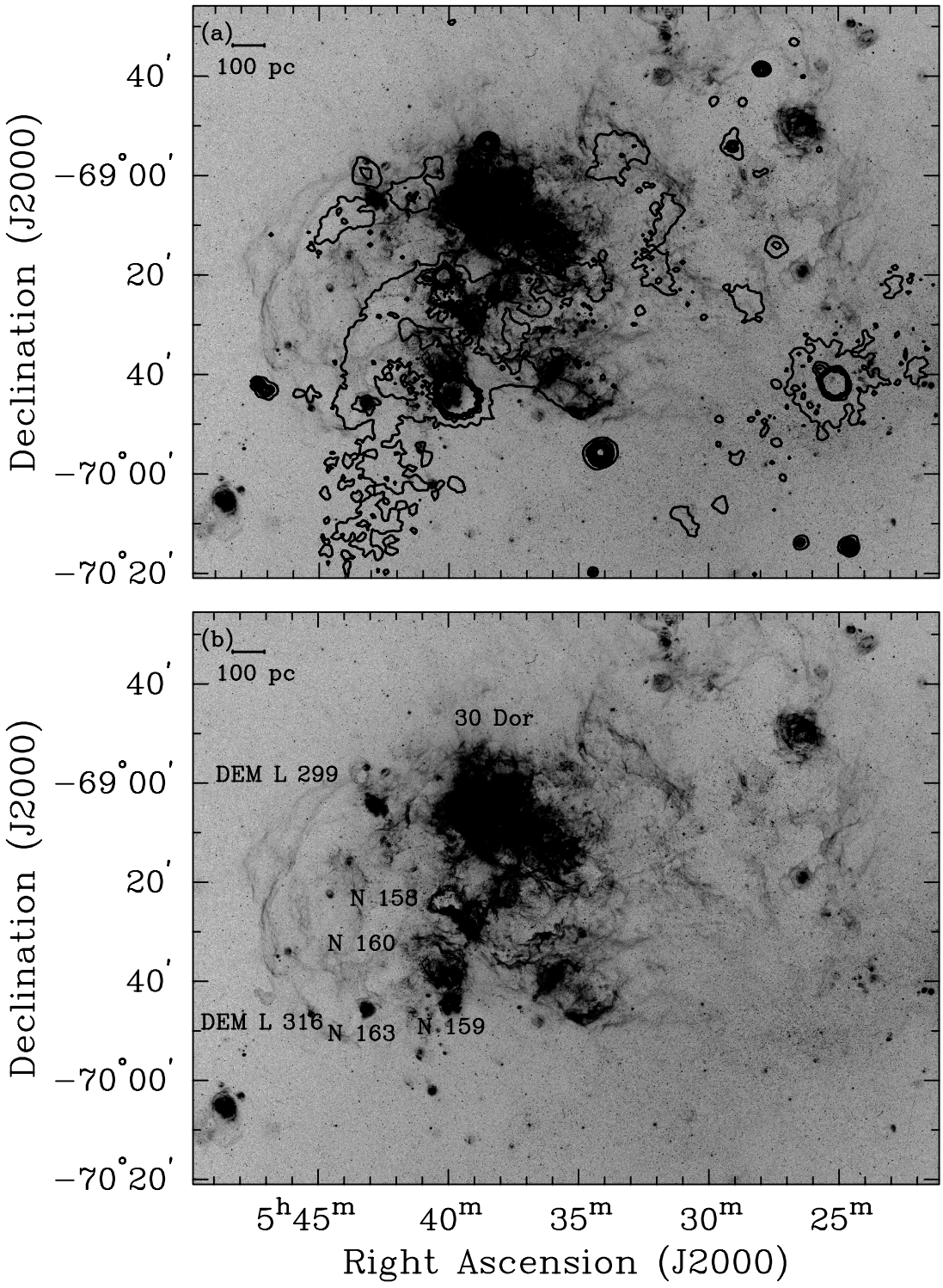

FIG. 2.—(*a*) PDS Hα image of LMC 2 and the surrounding region with PSPC contours overlaid (courtesy R. Kennicutt). The contour levels are in increments of 2×10^{-3} counts, starting at 2×10^{-3} s^{-1} and ending at 2×10^{-2} arcmin^{-2}. (*b*) Same as (*a*) with H II regions and SNRs mentioned in the text labeled.

south of LMC 2, as well as SNRs (e.g., DEM L 299, DEM L 316, and SNR 0540−69.3) and an X-ray binary (LMC X-1). These features are labeled on our HRI mosaic in Figure 1*b*.

A cursory inspection of our PSPC and HRI mosaics reveals that the X-ray surface brightness of LMC 2 is not uniform. The brightest region of diffuse X-ray emission associated with LMC 2 is an arc in the southwestern quadrant that appears to extend from SNR 0540−693 to LMC X-1. A region of low X-ray surface brightness ($\alpha_{2000} = 5^h45^m$, $\delta_{2000} = -69°25'$) lies between this bright X-ray arc and a region of bright X-ray emission in the northeast. The observed variation in X-ray surface brightness can be attributed to nonuniform emission from LMC 2 and/or to nonuniform absorption of X-rays by intervening interstellar

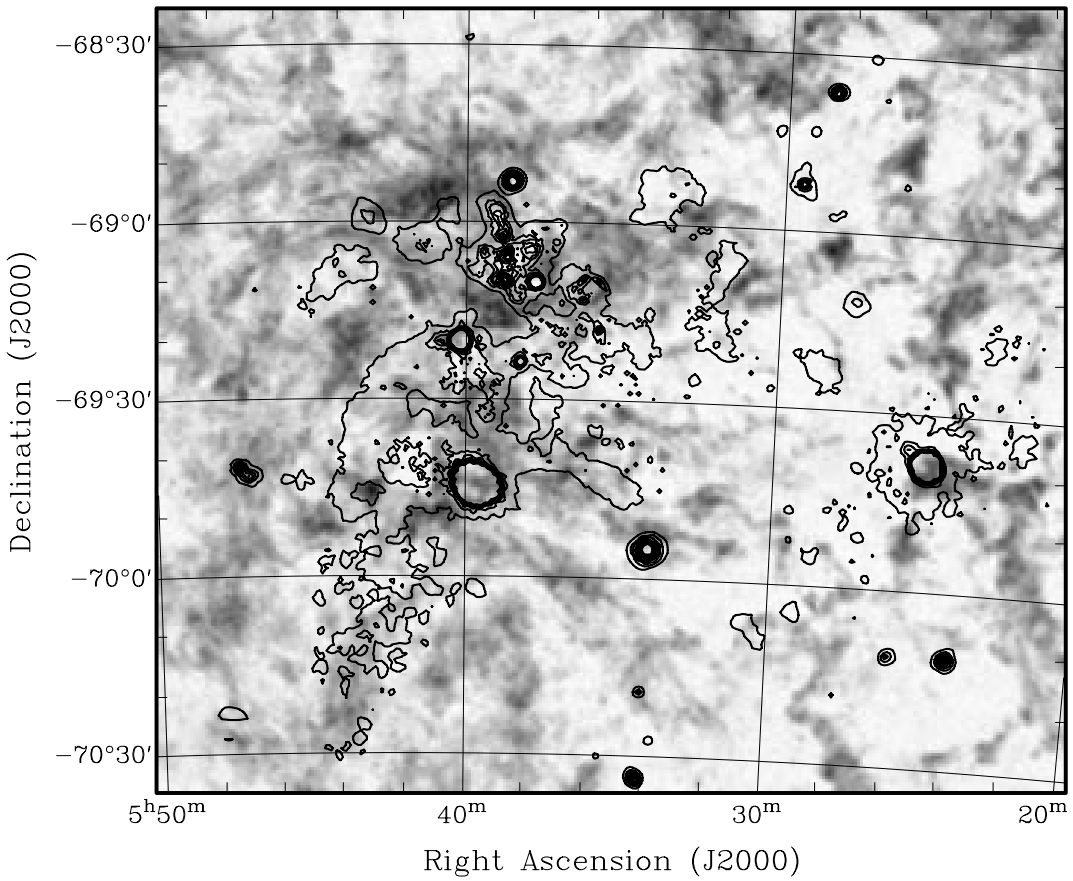

FIG. 3.—ATCA map of LMC 2 integrated over the velocity range of V_{hel} = 190–387 km s^{-1} with PSPC contours overlaid. The contour levels are the same as in Fig. 2*a*. The peak temperature of the plotted H I map is 99 K.

gas. As discussed below, we find that both of these explanations must be taken into account for the observed X-ray surface brightness toward LMC 2.

3.2. *Comparison of X-Ray Images with Optical/Radio Observations*

It is of considerable importance in our study of the physical conditions interior of LMC 2 to determine whether the variation in X-ray surface brightness is the result of nonuniform absorption or emission. To investigate this matter, we first compare the X-ray mosaics with Hα emission line images that trace regions of current massive star formation. As the hot gas toward LMC 2 is most likely shock-heated by the stellar winds and supernova explosions of massive stars, we expect to see correspondence between X-ray and Hα features. We present an Hα image of LMC 2 overlaid with X-ray contours in Figure 2.

We find three results of note in this comparison. (1) The X-ray emission from LMC 2 is confined by the optical filaments. (2) The bright X-ray arc is centered on the H II region N160. Based on the optical and X-ray morphology and high-resolution echelle spectra of the Hα line, we suggest that the arc is formed by an outflow of hot gas from N160 into LMC 2 (Paper I). (3) The H II region N163 (α_{2000} = $5^h43^m09^s$, $\delta_{2000} = -69°45'54''$) is coincident with a small region of low X-ray surface brightness. Comparison of the PSPC mosaics (Snowden & Petre 1994) shows that this depression in X-ray surface brightness is more pronounced in the soft X-ray band (R4) than in the hard X-ray band (R7). Therefore, we conclude that N163 lies in front of the X-ray–emitting gas and absorbs the soft X-rays from LMC 2.

We further compare the X-ray mosaic with the Australia Telescope Compact Array (ATCA) aperture synthesis maps of the 21 cm H I emission line toward LMC 2 that reveals the presence of neutral atomic gas (Fig. 3). We know that H I exists in front and in back of LMC 2. Thus, we cannot simply expect variations in the H I column density to anticorrelate with the diffuse X-ray emission. Instead we use the shadowing effect to look for correlations between features in the H I channel maps with X-ray surface brightness. As reported in Paper I, a region of low X-ray surface brightness ($\alpha_{2000} = 5^h45^m$, $\delta_{2000} = -69°25'$) is coincident with an H I cloud detected in the H I channel maps. As in the case of the region with low X-ray surface brightness seen toward N163, this depression is more apparent in the R4-band mosaic than in the R7-band mosaic. Therefore, this H I gas component most likely lies on the front side of LMC 2 and absorbs the X-rays emitted from within LMC 2 (Paper I).

4. PHYSICAL CONDITIONS OF THE HOT GAS

The *ROSAT* PSPC and *ASCA* SIS data provide X-ray spectra of LMC 2 that can be used to derive the physical conditions of the hot gas. We will first describe the procedures used to perform the X-ray spectral fitting and the uncertainties involved. Then we will use the plasma temperature, foreground absorption column density, and X-ray emissivity obtained from the spectral fits to estimate the

electron density, surface mass density, and surface thermal energy density of the hot gas.

4.1. *X-Ray Spectral Fits*

The observed X-ray spectra are a convolution of the intrinsic spectra, the foreground absorption, and the detector response function. Because the foreground absorption and detector response are both energy dependent, we need to assume models of the intrinsic spectra and absorption cross sections to reduce the number of free parameters. We simulate the observed spectra by folding the assumed intrinsic emission and foreground absorption models with the detector response. The observed spectra are fitted by the simulated spectra; the χ^2 of the fits is used to determine the best fit.

The X-ray emission from LMC 2, as seen in the HRI mosaic (Fig. 1*b*), is truly diffuse, indicating a hot-plasma origin. Therefore, we adopt the Raymond & Smith (1977) thin plasma emission models for the intrinsic spectra. We use the Morrison & McCammon (1983) effective absorption cross sections per hydrogen atom to model the foreground absorption. The PSPC and SIS data were fitted separately because they were extracted from different regions toward LMC 2.

The spectral fitting of the *ASCA* SIS data was more difficult than the fitting of the *ROSAT* PSPC data. The SIS data were contaminated by scattered, high-energy photons from the bright nearby source LMC X-1, an X-ray binary with an accretion disk. Therefore, in the fitting procedure for the SIS data we added a power law and a blackbody disk component but held the values of the power-law photon index and the blackbody disk temperature constant at the values determined by Schlegel et al. (1994) for LMC X-1. We allowed the values of the Raymond-Smith plasma temperature and absorption column density to float to the best-fit values. This is not a perfect method to determine the plasma temperature and absorption column density of LMC 2 because the scattering of the X-ray photons is both energy dependent and position dependent. We may fit the SIS 0 chip 1 and SIS 1 chip 3 data simultaneously with the same model because these data were extracted from the same region on the sky.

We performed multiple model fits for each of the extracted regions using XSPEC in which we allowed the abundance to be 20%, 30%, and 40% solar. Although varying the abundance did not noticeably affect the best-fit values of the plasma temperature and absorption column density, it did change the parameter space of the χ^2 grid plots of the confidence contours. We find that the range of possible values for the plasma temperature and absorption column density are better constrained for the models with 40% solar abundance. For the remainder of this work, however, we use the results from the 30% solar abundance models, the canonical LMC value. Although our choice to use the best-fit values from the 30% solar abundance models may seem arbitrary, this allows us to compare our results with other studies of the hot, ionized medium in the LMC (§ 5). We note that the χ^2 grid plots for a thermal plasma with 40% solar abundance may cover a smaller area of parameter space because the hot gas has been enriched above the canonical LMC value through the actions of stellar winds and supernova explosions of massive stars.

We performed a χ^2 grid search of possible fits in order to determine the uncertainties in the fits for temperature (kT) and absorption column density ($N_{\rm H}$). The best-fit plasma temperature and absorption column density for a 30% solar abundance Raymond & Smith (1977) thermal plasma model for PSPC and SIS data, as well as the range of the 90% confidence contours, are given in the top section of Table 4. In Figures 4 and 5 we present the X-ray spectra of the different regions and their χ^2 grid plots for a thermal plasma with 30% solar abundance, respectively. The grid plots show the range of χ^2 fits for kT and $N_{\rm H}$ for each extracted region; the three contour levels represent the areas of 68%, 90%, and 99% confidence.

To better constrain the range of $N_{\rm H}$ and thus to better confine the range of plasma temperatures, we calculate the H I column density toward LMC 2. The Galactic values of $N_{\rm H}$ toward LMC 2 are $\sim 6.5 \times 10^{20}$ cm^{-2}, determined using the FTOOL "nh," which is derived from the H I map of Dickey & Lockman (1990). The LMC values of $N_{\rm H}$ toward LMC 2 are $\sim 4 \times 10^{21}$ cm^{-2} using the Parkes Multibeam H I Survey. The best-fit values of kT for the fixed $N_{\rm H}$ model fits, as well as the 90% confidence ranges for

TABLE 4

OBSERVED X-RAY PROPERTIES TOWARD LMC 2

Region	PSPC-North	PSPC-Arc	PSPC-Spur	SIS[a]
		Free $N_{\rm H}$ Fits		
kT[b] (keV)	0.14	0.23	0.17	0.32
$N_{\rm H}^{\rm b}$ (10^{22} cm^{-2}).....	0.87	0.67	0.62	0.32
kT[c] (keV).....	0.11–0.28	0.13–0.32	0.07–0.37	0.28–0.37, 0.60–0.69
$N_{\rm H}^{\rm c}$ (10^{22} cm^{-2}).....	0.58–1.08	0.48–0.94	0.12–1.43	0.24–0.42, 0.19–0.24
		Fixed $N_{\rm H}$ Fits		
kT[b] (keV)	0.31	0.33	0.23	0.29
$N_{\rm H}^{\rm d}$ (10^{22} cm^{-2}).....	0.48	0.43	0.42	0.47
kT[c] (keV).....	0.09–0.67	0.10–0.47	0.08–0.45	0.27–0.33, 0.60–0.69
$N_{\rm H}^{\rm c}$ (10^{22} cm^{-2}).....	0.08–1.25	0.28–1.05	0.07–1.35	0.34–0.54, 0.12–0.17

[a] Combined model fit of the SIS 0 chip 1 and SIS 1 chip 3 spectra.
[b] Parameter value is the best-fit value of the model.
[c] Parameter range gives 90% confidence levels.
[d] Parameter value is the sum of the Galactic and LMC components of $N_{\rm H}$ toward LMC 2 as given by Dickey & Lockman 1990 and L. Staveley-Smith 2000, unpublished, respectively.

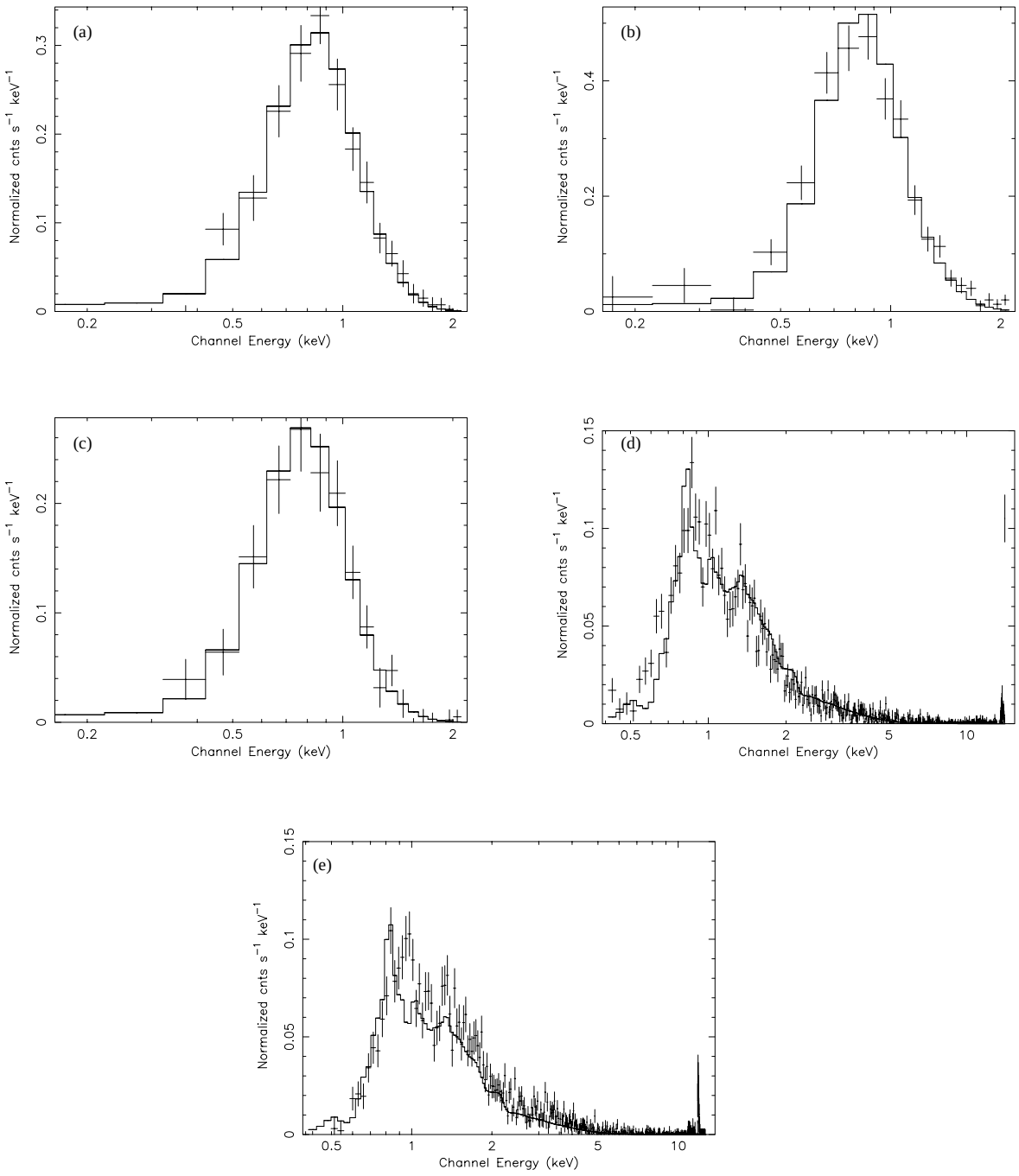

FIG. 4.—X-ray spectra and floating N_H model fits for the (*a*) PSPC-North, (*b*) PSPC-Arc, (*c*) PSPC-Spur, (*d*) SIS 0 chip 1, and (*e*) SIS 1 chip 3 regions. Both (*d*) and (*e*) were fitted simultaneously with the model but are shown here as separate plots for clarity.

kT and N_H, are given in the bottom section of Table 4. In general, the fixed N_H column density is lower than that determined by the floating N_H X-ray spectral fits (see Table 4), similar to results obtained toward 30 Doradus (Wang 1999). This appears to be problematic because the Parkes Multibeam Survey samples neutral H I that is both in front of and behind LMC 2. It seems reasonable that the fixed N_H column density should represent an upper limit of the absorption column density between us and the X-ray–emitting plasma. It should be remembered, however, that X-rays are also absorbed by molecular and ionized gas that are not measured in the 21 cm H I emission line survey but are measured by the X-ray spectral fits. Observations of the $J = 1$–0 CO emission line at 2.6 mm made with the NANTEN 4 m radio telescope (Fukui et al. 1999) do not show CO emission toward the LMC 2 regions of interest in this investigation. The lack of CO emission does not necessarily imply an absence of molecular gas toward the selected regions. The lower dust abundance of the LMC allows UV photons, which would dissociate CO molecules, to penetrate more deeply into molecular clouds and form C^+ regions. Observations of the [C II] 158 μm emission line toward LMC 2 reveal that the distribution of C^+ is more diffuse than the distribution of CO (Mochizuki et al. 1994).

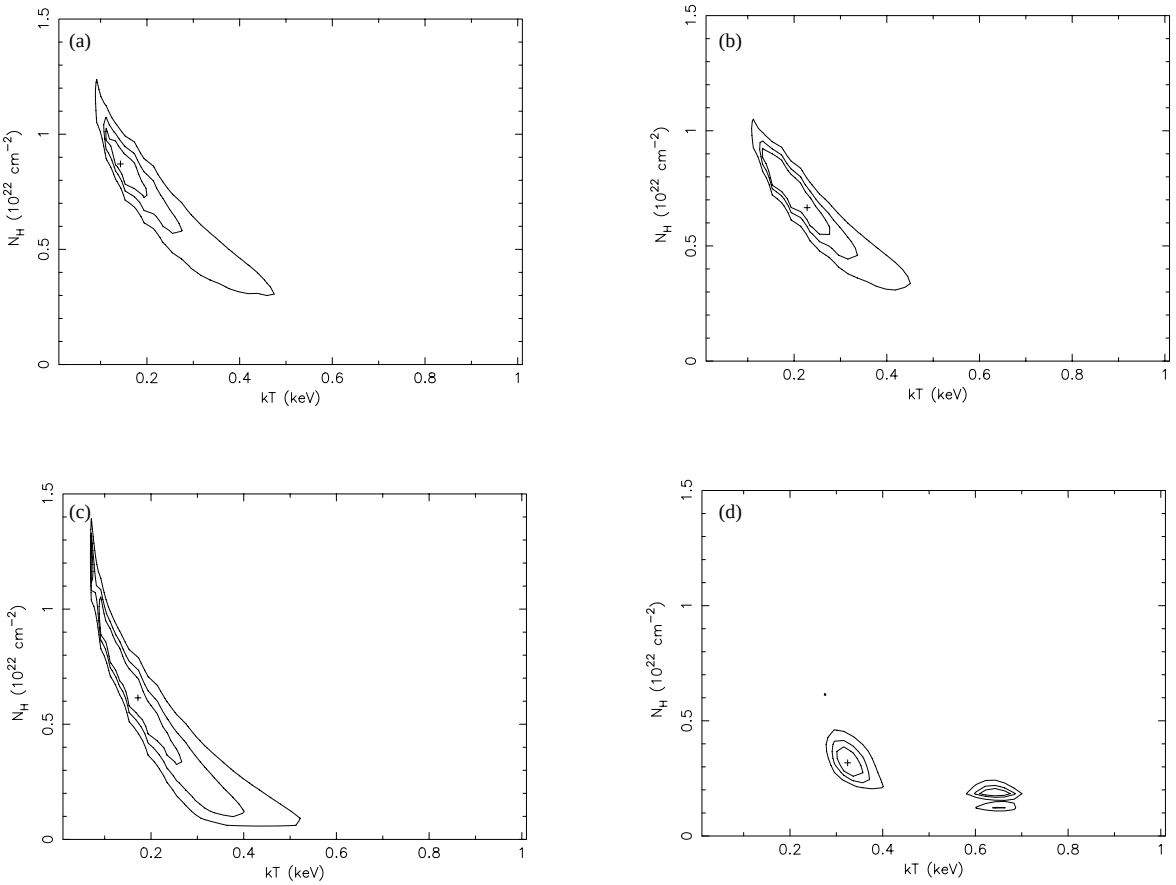

FIG. 5.—χ^2 grid plots for the (*a*) PSPC-North, (*b*) PSPC-Arc, (*c*) PSPC-Spur, and (*d*) SIS 0 chip 1 and SIS 1 chip 3 combined spectral fit. The three contours correspond to 68%, 90%, and 99% confidence levels. Temperatures are given in keV.

Therefore, it is possible that the molecular gas is in a very diffuse phase in which CO is rare because of photodissociation. Our calibrated CCD Hα images of LMC 2 (Paper 1) show the emission measure, $N_e^2 L$, where N_e^2 is the electron density and L is the path length through the Hα-emitting gas in pc, ranging from ~ 250 cm^{-6} pc in the arc region to ~ 20 cm^{-6} pc in the spur region. If the path length through the Hα-emitting gas is comparable to the width of the filaments defining the eastern boundary of LMC 2 (~ 5 pc), the ionized column densities toward the regions range from $N_{H^+} = 3.1 \times 10^{19}$ cm^{-2} in the spur to $N_{H^+} = 1.1 \times 10^{20}$ cm^{-2} in the arc. It is conceivable that the derived absorption column density from the free N_H X-ray spectral fits may be unrealistically higher than the measured absorption column density toward the X-ray spectral regions. Therefore, we use the fixed N_H spectral fit parameters for the remainder of this work.

4.2. *X-Ray Surface Brightness and Luminosity of LMC 2*

From the model fits to the PSPC and SIS X-ray spectra, we can calculate the unabsorbed X-ray flux, and hence the X-ray luminosities, of the selected regions. Given a hot gas filling factor f, volume V, X-ray luminosity L_X, and emissivity Λ, the electron density of the hot plasma of the selected regions will be

$$n_e = (1.1L_x)^{1/2}(\Lambda V f)^{-1/2} ,$$

if $n_e = 1.1 n_H$. For the regions toward LMC 2 and the spur, the volume of the gas is the product of the projected surface area of the region and the path length through the gas. We adopt a path length comparable to the width of the interstellar structure in question (i.e., 140 pc for the bright northern region, 230 pc for the bright X-ray arc, and 400 pc for the spur). The X-ray emissivity, Λ, is a function of the plasma temperature. From our fixed N_H X-ray model fits to the data, we find that the emissivity of the regions ranges from 5 to 7×10^{-24} ergs cm^3 s^{-1} in the 0.44–2.04 keV energy range. We derive the electron densities for the extracted regions toward LMC 2 using the X-ray luminosities and emissivities determined by our fixed N_H spectral fits and present them in Table 5.

As seen in Figure 1*a*, the X-ray surface brightness varies from region to region toward LMC 2. Because LMC 2 covers a large portion of the PSPC field of view, parts of it are obscured by the PSPC window support structure. Thus, we cannot extract a single X-ray spectrum of LMC 2 to determine the integrated X-ray flux of the hot gas. Instead, we determine the total count rate of LMC 2 from the PSPC mosaic in the 0.44–2.04 keV energy band. If we assume that LMC 2 is filled by hot gas with a plasma temperature $kT = 0.31$ keV and an absorption column density of $N_H = 4.5 \times 10^{21}$ cm^{-2}, we can use PIMMS[3] to calculate the intrinsic X-ray flux of LMC 2 to be 1.4×10^{-10} ergs cm^{-2} s^{-1}. The intrinsic X-ray flux of the spur is calculated to be 1.0×10^{-10} ergs cm^{-2} s^{-1} for a thermal plasma with tem-

[3] PIMMS is made available from HEASARC at http://heasarc.gsfc.nasa.gov/docs/software/tools/pimms.html.

TABLE 5

PHYSICAL PROPERTIES OF HOT GAS IN THE EXTRACTED REGIONS[a]

REGION NAME	l (pc)	F_X[b] (10^{-11} ergs cm^{-2} s^{-1})	L_X[b,c] (10^{36} ergs s^{-1})	Λ[b] (10^{-24} ergs cm^3 s^{-1})	n_e[d] (cm^{-3}) $f = 0.5$	n_e[d] (cm^{-3}) $f = 1.0$
PSPC-North.....	140	1.67	5.0	7.43	0.09	0.07
PSPC-Arc.....	230	1.92	5.7	7.75	0.08	0.06
PSPC-Spur	400	1.65	4.9	5.76	0.08	0.05
SIS[e].....	140	0.68	2.0	7.13	0.08	0.06

[a] Determined using the fixed N_H X-ray model fits given in Table 4.
[b] Measured in the 0.44–2.04 keV range (R4–R7 band).
[c] Assuming an LMC distance of 50 kpc.
[d] Derived using the assumed path length, l, and the projected surface area from Table 3.
[e] Derived using the combined X-ray model fits to the SIS data.

perature $kT = 0.22$ keV and a hydrogen absorption column density of $N_H = 4.5 \times 10^{21}$ cm^{-2}. We caution the reader, however, that these derived values of the X-ray flux were made assuming a uniform absorption column density between us and LMC 2 and the spur. Therefore, these values do not accurately reflect the global X-ray fluxes of either of these interstellar structures.

4.3. *Derived Physical Properties*

As X-ray fluxes have now been calculated for both LMC 2 and the spur, we may be tempted to derive their physical conditions, such as electron density (n_e), thermal energy (E_{th}), and hot gas mass (M). This approach, however, would ignore the uncertainties inherent in the assumptions we made in our previous calculation of the intrinsic X-ray flux of LMC 2 and the spur, such as the emitting volume, temperature, and the emissivity of the hot, thermal plasma. Furthermore, we have shown in § 3 that the absorption column density across LMC 2 is nonuniform. Therefore, the physical conditions of the hot gas interior to LMC 2 and the spur cannot be realistically derived using the global X-ray fluxes calculated in § 4.2. Instead, we opt to focus on the physical conditions of the hot gas toward the extracted spectral regions because the plasma temperatures, X-ray fluxes, and hot gas emissivities are explicitly determined by the X-ray spectral fits. To minimize uncertainties further in the derived physical conditions of the hot gas toward our extracted spectral regions, we calculate the surface thermal energy density ($\Sigma_{E_{th}}$) and the hot gas surface mass density (Σ_M) instead of E_{th} and M because they depend on the assumed path length through the hot gas, but not the volume.

In the following analysis we derive the physical properties of the hot gas in our selected regions toward LMC 2. As an example, we calculate the physical properties of the hot gas in the PSPC-Arc region. The electron density of this region is $n_e = 0.06$–0.08 cm^{-3}. The surface mass density of the hot gas is given by $\Sigma_M = 1.4 m_H n_H Vf/\Omega$, where Vf is the effective volume of the emitting gas and Ω is the surface area of the region in arcmin^2. Assuming that $n_e = 1.1 n_H$, the surface mass density of the hot gas in the arc ranges from 65 to 90 $M_\odot$ arcmin^{-2}. If the X-ray–emitting gas behaves as an ideal gas, the surface thermal energy density is given by $\Sigma E_{th} = \frac{3}{2} n_e VfkT/\Omega$. For the arc, this gives $\Sigma_{E_{th}} = (0.5$–$0.7) \times 10^{50}$ ergs arcmin^{-2}. Furthermore, we may also estimate the number of supernova explosions required to produce the hot gas interior to LMC 2, based on our derived value of $\Sigma_{E_{th}}$. For a supernova explosion with a total energy of 5.0×10^{50} ergs, the thermal energy of the hot gas of the SNR is 0.2×10^{50} ergs and has a radius of ~ 60 pc after 10^6 yr (Slavin & Cox 1992). At the distance to the LMC, the surface thermal energy density of the SNR would be $\Sigma_{E_{th}} \approx 0.004 \times 10^{50}$ ergs arcmin^{-2}. Thus, if the hot gas interior to LMC 2 was produced entirely by a series of supernova explosions $\approx 10^6$ yr ago, then the number of supernova explosions required to energize the arc is 125–175. We have obtained UBV photometry to investigate the star formation history toward LMC 2. Those data will allow us to determine the amount of energy massive stars have deposited in the ISM of LMC 2 and will be compared with the thermal energy that is derived here. The physical properties of the arc, as well as those for the other regions toward LMC 2, are presented in Table 6.

Before comparing the physical properties of the hot gas interior to LMC 2 with the physical properties of hot gas in other interstellar structures, we reiterate the assumptions that underlie our calculations. The first factor we consider that contributes to the uncertainty in our calculations is the volume of the X-ray–emitting gas in each of the regions. In this work we simply assume that the volume of a region is

TABLE 6

DERIVED PHYSICAL CONDITIONS OF THE HOT GAS[a]

Region	n_e (cm^{-3})	Σ_M ($M_\odot$)	$\Sigma_{E_{th}}$ (10^{50} ergs arcmin^{-2})	N_{SNe}
PSPC-North.....	0.07–0.09	46–65	0.32–0.46	80–115
PSPC-Arc.....	0.06–0.08	65–92	0.48–0.68	120–170
PSPC-Spur	0.05–0.08	107–152	0.56–0.79	140–198
SIS[b].....	0.06–0.08	41–58	0.27–0.38	68–95

[a] Results derived using the fixed N_H model X-ray spectral fits.
[b] Results from the combined SIS model fits.

the product of its projected surface area and the path length through the region. Because the depth through these regions is uncertain, an increase of the path length by a factor of 2 would alter our determination of the electron density by factor of $1/\sqrt{2}$ and our calculations of the surface thermal energy density and mass by a factor of $\sqrt{2}$. Another factor affecting the derivation of the physical properties of the hot gas interior to LMC 2 is the volume filling factor, f. We have determined the physical conditions of the hot gas using a filling factor of $f = 0.5$ and 1.0. A filling factor of $f = 0.5$ increases the derived values of n_e by a factor of $\sqrt{2}$ and decreases the values of $\Sigma_{E_{\rm th}}$ and Σ_M by a factor of $1/\sqrt{2}$, with respect to the values determined using a filling factor of $f = 1.0$. Inspection of Figures 1*a* and 1*b* reveals that the distribution of the X-ray emission is relatively smooth and does not show much structure. Thus, it is likely that the value of the filling factor of the hot gas interior to LMC 2 lies between these two bounds. The last factors that need to be considered as contributing to the uncertainty in our results are the best fits to the plasma temperature, kT, the absorption column density, $N_{\rm H}$, and the normalization constant, C, defined as $C = (10^{-14} \int n_e n_{\rm H}\, dV)/4\pi d^2$. As seen in the χ^2 grid plots (Fig. 5), the confidence contours for the PSPC data show that the thermal plasma spectrum can be fitted by a low plasma temperature and high absorption column density or by a high plasma temperature and a low absorption column density. For example, if we take the plasma temperature of the PSPC-North region to be the free $N_{\rm H}$ model best fit ($kT = 0.15$ keV, $N_{\rm H} = 8.6 \times 10^{21}$ cm^{-2}), the derived values of n_e and Σ_M are $\sim$7.5 times the values derived using the fixed $N_{\rm H}$ model fit values ($kT = 0.31$ keV, $N_{\rm H} = 4.8 \times 10^{21}$ cm^{-2}). In this example, the surface thermal energy density is $\sim$3.5 times the value calculated for the fixed $N_{\rm H}$ model fits and the intrinsic X-ray flux, $F_{\rm X}$, is increased by a factor of $\sim$20.

5. PHYSICAL PROPERTIES OF OTHER OBJECTS WITH DIFFUSE X-RAY EMISSION

The hot gas in the ISM is produced by shocks from supernova blasts and fast stellar winds from massive stars. Consequently, the amount of hot gas and its physical conditions depend upon the spatial distribution and formation history of massive stars. Massive stars will form discrete SNRs if they are isolated, superbubbles if there is a single burst of star formation such as an OB association, or supergiant shells if there are multiple bursts of star formation that have taken place over a period of time in a concentrated area. SNRs, superbubbles, and supergiant shells are all filled by hot gas, which contributes to the hot ionized medium (HIM; McKee & Ostriker 1977) component of the ISM in galaxies. Thus, it is of interest to compare the physical conditions of the hot gas in these interstellar structures.

Below we compare the physical properties of the hot gas interior to LMC 2 with those of (1) another supergiant shell in the LMC, LMC 4; (2) two superbubbles in the LMC, N11 and N44; and (3) a number of SNRs in the LMC. We present the physical properties of these objects in Table 7. The values of the physical properties for these objects were made using the *ROSAT* bandpass of 0.1–2.4 keV and assuming a hot gas filling factor of $f = 1.0$ unless otherwise noted.

5.1. *Supergiant Shells in the LMC*

The pioneering study of diffuse X-ray emission from within a supergiant shell in the LMC was performed on LMC 2 by Wang & Helfand (1991) using data obtained with the *Einstein* IPC, which operated in the energy range from 0.4 to 4.0 keV. Therefore, as a consistency check, we first compare our results of the physical conditions of the hot gas interior to LMC 2 to those that they derive. Because a detailed spectral analysis of LMC 2 could not be performed using the IPC data, Wang & Helfand (1991) used the mean hardness ratio of the excess X-ray emission from LMC 2 to estimate the temperature of the hot gas. By assuming an optically thin thermal plasma with 50% solar abundance for the emission and a foreground absorption of $N_{\rm H} \sim 3 \times 10^{21}$ cm^{-2}, they determine the temperature of the X-ray–emitting gas to be $\sim$0.43 keV. Wang & Helfand (1991) assume the geometry of LMC 2 to be spherical and adopt two different radii to determine the volume and physical properties of the 10^6 K gas: (1) a radius of 250 pc that covers only the arc region and (2) a radius of 500 pc

TABLE 7

PHYSICAL CONDITIONS OF HOT GAS IN OTHER OBJECTS IN THE LMC

Object Identification	kT (keV)	$F_{\rm X}$ (10^{-10} ergs cm^{-2} s^{-1})	n_e (cm^{-3})	$\Sigma_{E_{\rm th}}$ (10^{50} ergs arcmin^{-2})	Reference
LMC 2	0.43	0.4[a]	0.02[b]	0.46[b]	1
LMC 2	0.43	0.6[a]	0.009[c]	0.41[c]	1
LMC 4	0.21	0.5	0.008[d]	0.32[d]	2
N11	0.3	0.01	0.06[e]	0.23[e]	3
N44	0.55	0.02	0.14[f]	0.07[f]	4
DEM 316 A	0.8	0.009	0.28	0.16	5
DEM 316 B	0.9	0.007	0.15	0.08	5
N11 L	0.3	0.004	0.85	0.13	6
N86	0.15	0.008	0.16	0.03	6

[a] Measured in the *Einstein* bandpass of 0.4–4.0 keV.

[b] Derived using a radius of 250 pc covering the bright X-ray arc.

[c] Derived using a radius of 500 pc for the entire supergiant shell.

[d] Derived assuming that LMC 4 is cylindrical in shape with a radius of 600 pc and a height of 1200 pc.

[e] Derived assuming a radius of 60 pc for the superbubble and a hot gas emissivity of $\lambda = 3.5 \times 10^{-24}$ ergs cm^3 s^{-1}.

[f] Derived assuming a radius of 45 pc and a hot gas filling factor of $f = 0.5$.

REFERENCES.—(1) Wang & Helfand 1991. (2) Bomans et al. 1994. (3) Mac Low et al. 1998. (4) Magnier et al. 1996. (5) Williams et al. 1997. (6) Williams et al. 1999.

that encompasses the entire supergiant shell. They find the density of the hot gas to be $n_e \sim 2 \times 10^{-2}$ cm^{-3} or $n_e \sim 9 \times 10^{-3}$ cm^{-3} for an adopted radius of 250 or 500 pc. Their derived values of the unabsorbed X-ray flux, F_X, and the electron density, n_e, are given in Table 7. Using their derived values, we calculate the surface thermal energy density, $\Sigma_{E_{th}}$, to be 0.46×10^{50} and 0.41×10^{50} ergs arcmin^{-2} for a spherical bubble of hot gas with a radius of 250 and 500 pc, respectively.

The results obtained using the *Einstein* IPC data are in good agreement with those we determined using the *ROSAT* PSPC data, but not with the SIS data. For example, their values for the plasma temperature ($kT = 0.43$ keV) and the absorption column density ($N_H = 3 \times 10^{21}$ cm^{-2}) fall within the 90% confidence contour limits of our χ^2 grid plots of the PSPC data, but not the SIS data (see Fig. 5). A factor that may produce a discrepancy between the X-ray spectral fits to our data set and the analysis of the IPC data is that Wang & Helfand (1991) assume a uniform hydrogen column density toward LMC 2. We have shown in § 3.2 that the variations in X-ray surface brightness toward LMC 2 are caused by nonuniform absorption and emission. As discussed previously, a higher adopted absorption column density will result in a lower value for the plasma temperature. Therefore, it is likely that the differences between the observed spectral properties and the derived physical conditions can be attributed to the differences in the adopted absorption column density.

In addition to LMC 2, diffuse X-ray emission has also been detected in the northern quadrant of the supergiant shell LMC 4 (Bomans et al. 1994) using the *ROSAT* PSPC in the energy range between 0.1 and 2.4 keV. They find that the best-fit Raymond & Smith (1977) plasma temperature to the data is $kT = 0.21$ keV and the best-fit absorption column density is $N_H = 0.7 \times 10^{21}$ cm^{-2}. If the diffuse X-ray emission from the northern quadrant of LMC 4 is representative of LMC 4 as a whole, the X-ray flux is $\sim 5 \times 10^{-11}$ ergs cm^{-2} s^{-1} for this supergiant shell. Assuming that LMC 4 is a cylinder with a radius of 600 pc, a height of 1200 pc, and an X-ray emissivity of $\Lambda = 4.0 \times 10^{-24}$ ergs cm^3 s^{-1}, they derive an electron density of $n_e = 8 \times 10^{-3}$ cm^{-3}. Using these values we calculate the surface thermal energy density of LMC 4 to be $\Sigma_{E_{th}} = 0.32 \times 10^{50}$ ergs arcmin^{-2}. The derived values of F_X, n_e, and $\Sigma_{E_{th}}$ are listed in Table 7.

The plasma temperature of the hot gas interior to LMC 4 ($kT = 0.21$ keV) is comparable to what we have determined for LMC 2 at the 90% confidence level, but the absorption column density is about an order of magnitude lower. The primary distinction between the X-ray–emitting plasma in LMC 2 and LMC 4 is that the electron densities in the regions toward LMC 2 are a factor of ~ 10 greater than that derived for LMC 4. As we have used the same filling factor and a similar X-ray emissivity for the $\geq 10^6$ K gas as Bomans et al. (1994), the difference in the derived electron densities can be ascribed to the higher unabsorbed X-ray flux determined for LMC 2 and/or through uncertainties in the volume of the emitting thermal plasma. If we adopt a path length through our selected regions toward LMC 2 comparable to that of LMC 4 (i.e., $l = 1200$ pc), our derived electron densities would be lowered only by a factor of ~ 3–5. Therefore, we conclude that the electron density of the hot gas interior to LMC 2 is generally higher than the electron density interior to LMC 4.

5.2. *Superbubbles in the LMC*

Diffuse X-ray emission has been detected in several LMC superbubbles. Here we discuss the physical conditions of the hot gas interior to the superbubbles in N11 and N44, the two most luminous H II regions in the LMC after 30 Doradus (Kennicutt & Hodge 1986). N44 has the highest X-ray surface brightness among all superbubbles in the LMC (Chu & Mac Low 1990), while N11 is only moderately X-ray bright (Mac Low et al. 1998). The physical properties of the hot gas interior to these two superbubbles are given in Table 7.

Raymond & Smith (1977) spectral model fits to *ROSAT* PSPC observations of N11 give a best-fit plasma temperature of $kT = 0.3$ keV (Mac Low et al. 1998). This plasma temperature is higher than the model spectral fits to our PSPC data toward LMC 2 but is comparable to plasma temperatures determined by the model fits to the SIS data. Using their results, we calculate the electron density of N11 to be $n_e = 0.06$ cm^{-3} and the surface thermal energy density to be $\Sigma_{E_{th}} = 0.23 \times 10^{50}$ ergs arcmin^{-2}.

Both PSPC and SIS data have been obtained for N44 (Magnier et al. 1996). Because these observations cover the same region on the sky, the PSPC and SIS X-ray spectra were fitted simultaneously with a thermal plasma emission model. The model fits give a plasma temperature of $kT = 0.55$ keV for the hot gas interior to N44 (Magnier et al. 1996). Assuming a filling factor of $f = 0.5$, they derive an electron density of $n_e = 0.14$ cm^{-3} from which we calculate the surface thermal energy density to be $\Sigma_{E_{th}} = 0.07 \times 10^{50}$ ergs arcmin^{-2}.

The plasma temperatures of the hot gas interior to N11 are similar to those we determine for the hot gas interior to LMC 2 using the PSPC and SIS data but are higher in N44. The electron density and surface thermal energy density for N11 are on the same order as for the regions toward LMC 2. The electron density of the hot gas interior to N44 is a factor of ~ 1.5–3 times higher than that derived for LMC 2, but the surface thermal energy density is ~ 4–11 times lower. Some of the difference between the derived physical conditions of the hot gas interior to LMC 2 and N44 may be attributed to the fact that Magnier et al. (1996) used a hot gas filling factor of $f = 0.5$. The effects of changing the filling factor from $f = 1.0$ to $f = 0.5$ are discussed in § 4.3.

5.3. *SNRs in the LMC*

Supernova explosions are the main producers of the HIM in galaxies. Therefore, it is imperative to understand the physical properties of the hot gas interior to SNRs, in order to understand the physical conditions of hot gas interior to superbubbles and supergiant shells. Fortunately, the LMC contains a large number of SNRs (~ 40; Williams 1999) that have been studied extensively at optical and radio wavelengths (Mathewson et al. 1983, 1984, 1985) and at X-ray wavelengths (Williams et al. 1997, 1999; Williams 1999; Hughes, Hayashi, & Koyama 1998). Williams (1999) has compiled the most comprehensive list of the X-ray properties of LMC SNRs to date. Of the LMC SNR sample, 23 have *ROSAT* PSPC data available with sufficient count rates for spectral modeling. For this data set, Williams (1999) finds that the plasma temperature ranges from $kT = 0.14$ to 0.89 keV and that the electron density ranges from $n_e = 0.05$ to ~ 20 cm^{-3}. The published physical conditions of four of these SNRs are listed in Table 7.

Clearly, the hot gas interior to SNRs in the LMC shows a wide range of physical conditions. This is not surprising as they have different ages and interstellar environments. We see that most of these LMC SNRs have plasma temperatures that are higher than LMC 2 but have electron densities that are comparable to it.

6. SUMMARY

The supergiant shell LMC 2 has the highest X-ray surface brightness of all LMC supergiant shells. We have obtained *ROSAT* PSPC and HRI mosaics to study the distribution of X-ray emission from LMC 2. Comparison of the X-ray mosaics with Hα images shows that the X-ray emission is detected within the shell boundary of LMC 2, indicating the presence of hot ($\geq 10^6$ K) gas. In general, regions of low X-ray surface brightness are well correlated with regions of high H I column density, suggesting that some of the variations in X-ray surface brightness toward LMC 2 are caused by nonuniform absorption.

In addition to the X-ray mosaics, we have also obtained *ROSAT* PSPC and *ASCA* SIS X-ray spectra to determine the physical conditions of the hot gas interior to LMC 2. Model fits of an optically thin thermal plasma (Raymond & Smith 1977) to the X-ray spectra of selected regions show that the hot gas has a plasma temperature $kT = 0.1$–0.4 keV with a best fit of $kT \sim 0.3$ keV for our PSPC and SIS data. The electron density of the hot gas varies from $n_e \sim 0.05$ to 0.09 cm^{-3}. The unabsorbed X-ray flux in the 0.44–2.04 keV band is 1.4×10^{-10} ergs cm^{-2} s^{-1}.

We have compared the physical properties of LMC 2 with other supergiant shells, superbubbles, and SNRs in the LMC. The derived electron densities of the LMC 2 regions are generally comparable to the values determined for the supergiant shell LMC 4 and the superbubble N11 but are lower than those determined for the superbubble N44 and a sample of SNRs in the LMC. The plasma temperature of LMC 2 is comparable to that determined for LMC 4 and N11 but is generally lower than the plasma temperatures determined for N44 and SNRs in the LMC.

This work is supported by NASA grants NAG 5-2973 and NAG 5-8104. This research has made use of data obtained from the High Energy Astrophysics Science Archive Research Center (HEASARC), provided by the NASA Goddard Space Flight Center. S. D. P. wishes to thank J. Turner for many helpful discussions on the reduction of *ROSAT* PSPC data using XSPEC. S. D. P. also wishes to thank Q. D. Wang for his helpful comments.

APPENDIX

ROSAT-POINTED OBSERVATIONS TOWARD LMC 2

Here we present Tables A1 and A2, which list the individual *ROSAT*-pointed observations that were mosaicked to produce the PSPC and HRI mosaics, respectively. These tables contain the number of data sets for each observation, the pointing direction, exposure time, and target name.

TABLE A1

PSPC OBSERVATIONS INCLUDED IN MOSAIC

Sequence	Sets[a]	R.A. (J2000)	Decl. (J2000)	Exposure (ks)	Target
500138.....	2	5 26 36	−68 50 23	27.08	N144
400148.....	1	5 27 47	−69 54 00	5.90	RX J0527.8−6954
400298.....	2	5 27 47	−69 54 00	14.85	RX J0527.8−6954
300172.....	3	5 32 28	−70 21 36	12.54	Nova LMC 88 #1
500100.....	2	5 35 28	−69 16 11	24.84	SN 1987A
500303.....	1	5 35 28	−69 16 11	9.16	SN 1987 A
600100.....	1	5 35 38	−69 16 11	12.16	Region F
300335.....	1	5 36 12	−70 45 00	9.90	Two new supersoft SRCs
500131.....	1	5 38 33	−69 06 36	15.45	N157
400079.....	1	5 39 38	−69 44 23	5.20	LMC X-1
150044.....	1	5 40 12	−69 19 48	5.15	PSR 0540−69
400052.....	1	5 40 12	−69 19 48	6.55	PSR 0540−69
400133.....	1	5 40 12	−69 19 48	1.72	PSR 0540−69
400012.....	1	5 46 45	−71 09 00	14.92	CAL 87
400013.....	1	5 46 45	−71 09 00	14.73	CAL 87
500259.....	1	5 47 09	−69 41 59	3.92	DEM 316

NOTE.—Units of right ascension are hours, minutes, and seconds, and units of declination are degrees, arcminutes, and arcseconds.

[a] Number of separate data sets processed for observation.

TABLE A2

HRI Observations Included in Mosaic

Sequence	Sets[a]	R.A. (J2000)	Decl. (J2000)	Exposure (ks)	Target
400124.....	1	5 18 40.8	−68 14 24	4.55	LMC H204
500171.....	3	5 19 33.6	−69 02 24	17.32	0519.69.0
400657.....	1	5 20 31.2	−69 31 48	3.83	RX J0520.5−6932
400153.....	2	5 22 26.4	−67 58 12	8.56	N44C/STAR 2
400231.....	1	5 22 28.8	−69 26 24	3.89	LMC field 1
600036.....	1	5 22 33.6	−69 18 36	1.13	LMC H20
500002.....	1	5 25 2.4	−69 38 24	27.25	N132D
600032.....	1	5 25 43.2	−69 13 12	0.71	CAL 37
600031.....	1	5 25 52.8	−70 11 24	1.26	CAL 38
400353.....	2	5 26 9.6	−67 42 36	7.94	LMC field A
400238.....	1	5 26 28.8	−69 46 48	3.99	H211
600033.....	1	5 27 38.4	−69 10 48	1.65	CAL 40
201689.....	1	5 27 48	−69 54 00	8.50	RX J0527.8−6954
600647.....	1	5 28 19.2	−68 30 36	23.91	LMC point 017
600646.....	1	5 28 19.2	−68 51 00	24.01	LMC point 016
600641.....	1	5 28 19.2	−69 10 48	26.71	LMC point 011
600782.....	1	5 28 19.2	−69 51 00	12.79	LMC point AO6-10
400356.....	1	5 28 33.6	−68 36 36	3.16	W528.8−684
400355.....	1	5 28 43.2	−67 25 48	4.60	W529.8−672
600777.....	1	5 28 50.4	−69 33 00	19.84	LMC point AO6-05
600645.....	1	5 32 4.8	−68 30 36	19.00	LMC point 015
600640.....	1	5 32 4.8	−68 51 00	23.98	LMC point 010
600635.....	1	5 32 4.8	−69 10 48	21.23	LMC point 005
600655.....	1	5 32 4.8	−70 10 48	11.99	LMC point 026
400125.....	1	5 32 7.2	−69 19 12	4.92	LMC H215
400660.....	1	5 32 16.8	−71 40 12	5.52	RX J0532.3−7140
400234.....	2	5 32 52.8	−67 43 12	6.39	LMC field 2
500234.....	1	5 33 60	−69 55 12	7.66	0534−69.9
400352.....	2	5 35 4.8	−70 39 00	5.43	LMC field B
400056.....	1	5 35 28.8	−69 16 12	23.47	SN 1987A
600634.....	1	5 35 52.8	−68 51 00	23.62	LMC point 004
600650.....	1	5 35 52.8	−69 51 00	2.10	LMC point 020
400230.....	1	5 35 55.2	−69 21 00	4.86	LMC field 3
400233.....	1	5 35 55.2	−69 56 24	4.98	LMC field 4
600035.....	1	5 36 2.4	−67 34 48	0.78	CAL 60
600639.....	1	5 36 7.2	−68 31 48	25.62	LMC point 009
400644.....	1	5 36 16.8	−67 18 00	4.57	RX J0536.3−6718
500036.....	1	5 37 52.8	−69 10 12	10.91	N157B
400642.....	1	5 38 16.8	−69 24 00	2.43	CAL 69
600228.....	1	5 38 43.2	−69 06 00	30.09	30 DOR
400649.....	1	5 38 52.8	−69 01 48	2.72	CAL 74
600638.....	1	5 39 38.4	−68 30 36	25.73	LMC point 008
600633.....	1	5 39 38.4	−68 51 00	21.50	LMC point 003
150013.....	1	5 39 38.4	−69 44 24	0.80	LMC X-1
400650.....	1	5 39 43.2	−69 45 00	1.20	LMC X-1
600774.....	1	5 40 4.8	−69 31 48	22.34	LMC point AO6-02
150008.....	1	5 40 12	−69 19 48	21.59	SNR 0540−69.3
400236.....	1	5 40 45.6	−70 12 00	1.55	LMC field 6
400349.....	2	5 41 26.4	−68 49 48	6.56	LMC field C
500235.....	1	5 43 7.2	−68 58 48	28.24	0543−68.9
600643.....	1	5 43 26.4	−68 30 36	21.45	LMC point 013
600632.....	1	5 43 26.4	−68 51 00	22.49	LMC point 007
600637.....	1	5 43 26.4	−68 51 00	22.49	LMC point 007
600773.....	1	5 43 26.4	−69 30 36	15.99	LMC point AO6-01
600648.....	1	5 43 26.4	−69 51 00	1.50	LMC point 018
600778.....	1	5 43 26.4	−69 51 00	8.79	LMC point AO6-06
400121.....	1	5 46 28.8	−68 34 12	1.59	CAL 86
400123.....	1	5 46 57.6	−68 52 12	1.39	LMC H232
500232.....	2	5 47 9.6	−69 42 00	20.35	0547−69.7
600644.....	1	5 47 12	−68 30 36	18.76	LMC point 014
600642.....	1	5 47 12	−68 51 00	21.10	LMC point 012
600636.....	1	5 47 12	−69 10 48	20.63	LMC point 006
600631.....	1	5 47 12	−69 30 36	25.65	LMC point 001
500233.....	2	5 47 50.4	−70 24 36	26.41	0548−70.4
400659.....	1	5 47 52.8	−68 22 48	5.29	RX J0547.9−6823

Note.—Units of right ascension are hours, minutes, and seconds, and units of declination are degrees, arcminutes, and arcseconds.

[a] Number of separate data sets processed for observation.

REFERENCES

Bessell, M. S. 1991, A&A, 242, L17
Bomans, D. J., Dennerl, K., & Kürster, M. 1994, A&A, 283, L21
Chu, Y.-H., & Mac Low, M.-M. 1990, ApJ, 365, 510
Chu, Y.-H., & Snowden, S. L. 1996, in *ROSAT* Newsletter 13, ed. S. L. Snowden (NASA: GSFC), 26
Dickey, J. M., & Lockman, F. J. 1990, ARA&A, 28, 215
Feast, M. 1999, PASP, 111, 775
Fukui, Y., et al. 1999, PASJ, 51, 745
Goudis, C., & Meaburn, J. 1978, A&A, 68, 189
Greisen, E. W., & Calabretta, M. 1995, in ASP Conf. Ser. 77, Astronomical Data Analysis Software and Systems IV, ed. R. A. Shaw, H. E. Payne, & J. J. E. Hays (San Francisco: ASP), 223
Henize, K. G. 1956, ApJS, 2, 315
Hughes, J. P., Hayashi, I., & Koyama, K. 1998, ApJ, 505, 732
Kennicutt, R. C., & Hodge, P. W. 1986, ApJ, 306, 130
Kuntz, K. D., & Snowden, S. L. 1998, Cookbook for Analysis Procedures for *ROSAT* XRT Observations of Extended Objects and the Diffuse Background, Part II: Mosaics, US *ROSAT* Science Data Center (NASA: GSFC)
Mac Low, M.-M., Chang, T. H., Chu, Y.-H., Points, S. D., Smith, R. C., & Wakker, B. P. 1998, ApJ, 493, 260
Magnier, E. A., Chu, Y.-H., Points, S. D., Hwang, U., & Smith, R. C. 1996, ApJ, 464, 829
Mathewson, D. S., Ford, V. L., Dopita, M. A., Tuohy, I. R., Long, K. S., & Helfand, D. J. 1983, ApJS, 51, 345
Mathewson, D. S., Ford, V. L., Dopita, M. A., Tuohy, I. R., Mills, B. Y., & Turtle, A. J. 1984, ApJS, 55, 189
Mathewson, D. S., Ford, V. L., Tuohy, I. R., Mills, B. Y., Turtle, A. J., & Helfand, D. J. 1985, ApJS, 58, 197
McKee, C. F., & Ostriker, J. P. 1977, ApJ, 218, 148
Meaburn, J. 1980, MNRAS, 192, 365
Mochizuki, K., et al. 1994, ApJ, 430, L37
Morrison, R., & McCammon, D. 1983, ApJ, 270, 119
Points, S. D., Chu, Y.-H., Kim, S., Smith, R. C., Snowden, S. L., Brandner, W., & Gruendl, R. A. 1999, ApJ, 518, 298 (Paper I)
Raymond, J. C., & Smith, B. W. 1977, ApJS, 35, 419
Schlegel, E. M., Marshall, F. E., Mushotzky, R. F., Smale, A. P., Weaver, K. A., Serlemitsos, P. J., Petre, R., & Jahoda, K. M. 1994, ApJ, 422, 243
Slavin, J. D., & Cox, D. P. 1992, ApJ, 392, 131
Snowden, S. L., & Kuntz, K. D. 1998, Cookbook for Analysis Procedures for *ROSAT* XRT Observations of Extended Objects and the Diffuse Background, Part 1: Individual Observations, US *ROSAT* Science Data Center (NASA: GSFC)
Snowden, S. L., McCammon, D., Burrows, D. N., & Mendenhall, J. A. 1994, ApJ, 424, 714
Snowden, S. L., & Petre, R. 1994, ApJ, 436, L123
Tanaka, Y., Inoue, H., & Holt, S. S. 1994, PASJ, 46, L37
Tenorio-Tagle, G., & Bodenheimer, P. 1988, ARA&A, 26, 145
Wang, Q. D. 1999, ApJ, 510, L139
Wang, Q. D., & Helfand, D. J. 1991, ApJ, 379, 327
Williams, R. M. 1999, Ph.D. thesis, Univ. Illinois at Urbana-Champaign
Williams, R. M., Chu, Y.-H., Dickel, J. D., Beyer, R., Petre, R., Smith, R. C., & Milne, D. K. 1997, ApJ, 480, 618
Williams, R. M., Chu, Y.-H., Dickel, J. D., Smith, R. C., Milne, D. K., & Winkler, P. F. 1999, ApJ, 514, 798